Lithospheric layering beneath northern Central Africa by S-to-P receiver functions

Awad A. Lemnifi[1, 2], Lin Liu[3, 4], John Browning[5]

[1]Mining Engineering department, Missouri University of Science and Technology, Rolla, MO, USA.

[2]Department of Earth Science, Faculty of Sciences, Benghazi University, Libya.

[3]Key Laboratory of Submarine Geosciences and Prospecting Techniques, Ministry of Education, College of Marine Geosciences, Ocean University of China, Qingdao, China.

[4]Department of Geophysics, Stanford University, Stanford, CA, USA.

[5]Department of Mining Engineering and Department of Structural and Geotechnical Engineering, Pontificia Universidad Catolica de Chile, Santiago, Chile.

Corresponding author: Lin Liu (lltrc@mst.edu)

Abstract

Using a total of 4,520 S-to-P receiver functions (SRFs) recorded by 19 broadband seismic stations belonging to the Libyan Center for Remote Sensing and Space Science and the Incorporated Research Institutions for Seismology Data Management Center, we imaged the depth of the lithosphere–asthenosphere boundary (LAB) beneath northern Central Africa. This boundary occurs over the depth range of 57–124 km which we imaged in consecutive circular bins (radius of 2°) using a high number of receiver functions. The mean depth of the discontinuity is 80 ±17 km, which is significantly shallower than the global average of ~250 km, commonly found beneath ancient cratons. The SRFs in the study area produced 156 bins with observable arrivals from the LAB. All the stacked traces were plotted along eight latitudinal profiles from 20°N to 35°N. The observed depth of the LAB increases systematically toward the northern central part of the study area from approximately 67 km to 120 km. The apparent depth of the LAB increases from 70 to 90 km from 21°N to 28°N and then further increases to 120 km from 28°N to 34°N. These depth variations are extreme beneath the northern central part of Libya. The LAB depth

26 beneath the Hoggar volcanic province area is relatively low (~57 km) compared to other areas. This study

27 provides new constraints on regional-scale tectonic processes such as lithospheric stretching or thinning,

28 due to partial melting beneath the study region that may be an effect of the LAB topography in this part

29 of northern Central Africa.

30

1. Introduction

32   Mapping and understanding the depth and physical properties of the lithosphere-asthenosphere

33 boundary (LAB) is essential for interpreting processes occurring within the upper mantle structure, the

34 tectonics of lithospheric plates, and the evolution of the Earth (McKenzie and Priestley, 2008; Liu and

35 Gao, 2018). In addition, the variations in the depth of the LAB within cratons and extensional provinces

36 can provide further details about the mechanisms driving the behavior of tectonic plates (e.g., Abt et al.,

37 2010). The base of the lithosphere, i.e., the LAB, and the mid-lithospheric discontinuity (MLD) have been

38 detected in different regions using negative velocity contrasts (e.g., Fischer et al., 2010; Liu and Gao,

39 2018; Wirth and Long, 2014).

40   The lithosphere of North Africa has a rich tectonic history that includes Pan-African orogenesis,

41 volcanism, subduction, and present-day extension in the Sirte Basin (e.g., Lemnifi et al., 2015; 2017;

42 2019) (Figure 1). Numerous global and regional tomographic studies (e.g., Marone et al., 2003; Li´egeois

43 et al., 2005; Pasyanos and Nyblade, 2007; Montagner et al., 2007; Fishwick, 2010; Bardintzeff et al.,

44 2012) have shown weak velocity anomalies, but the depths of their investigations were limited. Volcanic

45 provinces throughout northern Central Africa (Figure 1) are mainly associated with negative Bouguer

46 anomalies, and the lithospheric thickness indicated from surface wave tomography is relatively thin,

47 approximately 90 to 100 km (Fishwick, 2010).

To investigate the lithospheric thickness and discontinuities within the lithosphere, two essential seismological techniques are used: surface wave tomography (McKenzie and Priestley, 2008; Bedle and Van Der Lee, 2009; Schaeffer and Lebedev, 2014; Caló et al., 2016; Liu and Gao 2018) and receiver function (RF) stacking (Rychert and Shearer, 2009; Fischer et al., 2010; Kind et al., 2012; Liu and Gao, 2018). The most common technique employed to image the Moho is the P-to-S RF method (Zhu and Kanamori, 2000; Gao and Liu, 2014; Liu et al., 2017; Lemnifi et al., 2019). This method has disadvantages in imaging the LAB; for example, strong Moho multiples appear within the expected time window of the arrivals associated with the discontinuities of interest (Faber and Müller, 1980; Liu and Gao, 2018). However, the most important benefit of SRFs is that they are less affected by crustal reverberations, which tend to obscure the LAB (e.g., Eaton et al., 2009).

A number of studies have been performed using the SRF method (for a recent summary, see Kind et al., 2012; Liu and Gao, 2018) to determine the LAB. For example, a sharp negative-wave speed discontinuity (NVD) was observed in the depth range of 40–180 km; this NVD, which is regarded as an MLD or the LAB, was previously studied by Fishwick (2010) using a global velocity model. In recent decades, seismicity studies of northern Central Africa have mainly used global surface tomography models, revealing that the lithospheric thickness beneath Central Africa ranges from 90 km to 100 km, especially beneath volcanic provinces. Lemnifi et al. (2017) suggested that the thinning of the lithosphere may be due to the presence of partial melt and currently active magma reservoirs, which were detected by observing low Vp/Vs ratios obtained through H-k stacking.

Here we use all available seismic data within the study region to investigate the LAB depth therein. For this purpose, we utilize all the recorded data from broadband seismic stations belonging to the Libyan Center for Remote Sensing and Space Science (LCRSSS) and stations that are publicly available and archived by the Incorporated Research Institutions for Seismology (IRIS) Data Management Center

(DMC) to image the depth of the LAB and stacking amplitude associated with lithospheric discontinuities (relative to the direct S wave) beneath northern Central Africa.

2. Method

The data used in this study were requested from the LCRSSS with a recording period ranging from early 2005 to late 2010. Additionally, we requested data recorded by 3 public broadband seismic stations located in the region between the latitudes of 25°N and 36°N and the longitudes of 4°E and 25°E from the IRIS DMC.

2.1   Receiver function stacking

Seismic events with epicentral distances ranging from 60° to 85° were selected based on a varying cut-off magnitude, which was determined by the epicentral distance and focal depth, as defined by Yuan et al. (2006) and Liu and Gao (2010). The seismograms were windowed starting 180 s prior to and extending to 20 s after the first theoretical S-wave arrival according to the IASP91 Earth model. After being bandpass filtered within the frequency band from 0.04 to 0.40 Hz, all of the events that demonstrate a signal-to-noise ratio (S/N) of 1.5 or greater on the radial component were selected. The cutoff magnitude was determined by the epicentral distance and focal depth as defined by Liu and Gao (2010) using the following equation:

$$Mc=5.2+(De-30.0)/(180.0-30.0)-Hf/700 \qquad (1)$$

where De is the epicentral distance between 60° and 85°, for this study, and Hf is the focal depth in km. To isolate converted Sp waves from direct S waves, the ZRT components are rotated into an LQT (P, Sv, Sh) ray-based coordinate system, in which the L component is in the direction of the incident S wave, the Q component is perpendicular to the L component and is positive away from the source, and the T

component is the third component of the LQT right-hand system. In order to eliminate the influences of the source and ray path, an equalization procedure is applied by deconvolving the L and T component seismograms with the S signal on the Q component. The resulting L component data are known as Sp receiver functions, which are mainly composed of the S-to-P converted energy and contain information on the structure beneath a seismic station. A total of 4,520 SRFs were used in the study area.

We stacked the moveout-corrected RFs within circular bins, each with a radius of 2°, based on the locations of the ray-piercing points at a depth of 150 km (Dueker and Sheehan, 1997). The IASP91 reference Earth model (Kennett and Engdahl, 1991) was employed to calculate the stacked receiver functions with a non-plane wave-front assumption (Gao and Liu, 2014). The moveout procedure employed to correct and stack the SRFs follows a common conversion point (CCP) approach (Dueker and Sheehan, 1997; Liu and Gao, 2018). The moveout correction was applied to stack the SRFs using the following equation (Sheriff and Geldart, 1982; Dueker and Sheehan, 1997; Liu and Gao, 2018) to remove the influence of the ray parameter on the arrival times.

$$T_{sp}\text{-}T_s = \int_{-h}^{0}\left[\sqrt{(V_s(z)^{-2} - p^2)} - \sqrt{V_p(z)^{-2} - p^2}\right]dz \qquad (2)$$

where p is the S-wave ray parameter, h is the depth of the candidate discontinuity (ranging from 0 to 300 km), and Vp (z) and Vs (z) are the P- and S-wave velocities, respectively, at the depth z. Stacked traces determined by fewer than 5 RFs were rejected in this study. To increase the reliability of the results, we manually picked the maximum amplitude near the theoretical arrival of the converted P waves from the LAB.

3. Results

The SRFs in the study area produced 156 bins with observable arrivals from the LAB (see Table 1 for all measurements). The depths of the NVD and the corresponding stacking amplitudes are shown in Table 1. All the stacked traces plotted along eight latitudes from 21°N to 34°N are shown in Figures 4 and 5 and Figures S1 and S2. The observed depth of the LAB increases systematically toward the northern central study area from approximately 70 km to 120 km (Figure 4). The apparent depth of the LAB increases from 70 to 90 km from latitudes 21° to 28° and then increases to 124 km from latitudes 28° to 34°. The changes in the LAB depth are extreme beneath the northern central part of Libya (Figures 5 and 6). The depths of the LAB beneath the Hoggar volcanic province are relatively shallow compared with those in other areas, while the LAB depth increases beneath the northeastern portion of Libya. The resulting LAB depths in the southern part of the study region are shallow compared to those in the northern part of the study area; in other words, the LAB is especially shallow beneath the Hoggar volcanic province and the western margin of the Tibesti volcanic province. The LAB depth is slightly shallower than normal beneath the northeastern part of the region, as well as beneath the northwestern part of the study area, where the LAB depth ranges from 74 to 96 km with an average of 83 ± 5 km.

4. Discussion

The depth of the LAB beneath the study area appears to vary widely by a few tens of kilometers (Figures 5, 6, and 7). Parts of the study area, such as the Hoggar and Tibesti volcanic provinces, are characterized by a shallow discontinuity. The LAB was determined according to a significant negative velocity contrast. Some previous studies (e.g., Faul and Jackson, 2005; Stixrude and Lithgow-Bertelloni, 2005; Priestley and McKenzie, 2006; Abt et al., 2010) interpreted that the velocity is reduced from the lithosphere to the asthenosphere due to a temperature difference or a combination of temperature and grain size. In contrast, Lee (2003), Schutt and Lesher (2006) concluded that the decrease in the shear-wave

velocity can be attributed to partial melting. Comparing our results with some geodynamic prediction models (e.g., King and Ritsema, 2000; Korenaga and Jordan, 2002; Cooper et al., 2004) and the lithospheric layering model beneath the United States constrained by Liu and Gao (2018), who also used S-to-P receiver functions, the presence of varying velocities (Figures 5 and 6) likely indicates that the asthenosphere contains partial melt with a small amount of hydration relative to the lithospheric mantle. The larger amplitudes observed in Figures 5 and 6 could also be due to lower asthenospheric velocities. These larger amplitudes were similarly observed elsewhere, such as in the Vs model by Yuan and Romanowicz (2010), suggesting that the larger amplitude of the negative velocity contrast beneath the western United States is due to high temperatures, partial melt beneath the lithosphere, and a melt-free lithosphere. In addition, some other studies, such as that conducted by Anderson and Sammis (1970), suggested that the reduction in the seismic velocity may be caused by partial melting, which is consistent with our observation.

More recently, by using receiver function analysis, Lemnifi et al. (2019) found that the MTZ beneath the volcanic provinces in the study area is approximately 10 km thinner than normal. The average lithospheric thickness beneath the Hoggar volcanic province is ~10 km less than the normal thickness of 75 km, which is consistent with the elevation and Bouguer gravity anomalies (e.g., Parsons et al., 1994; Liu and Gao, 2010). The average LAB depths beneath the volcanic provinces throughout Libya, such as the Al Haruj, As Sawda, and Tibesti volcanic provinces, relative to the LAB depth beneath the Hoggar volcanic province suggest that the lithosphere beneath the Hoggar volcanic province is older that that beneath the others and has thus been subjected to more extension and thermal erosion. Therefore, we conclude that a possible mechanism contributing to the shallowing of the LAB is stretching of the lithosphere, which is caused by partial melting and the upwelling of hot materials from deep sources. In addition, Abdelsalam et al. (2002) and Lemnifi et al. (2015 and 2017) reported that the lower part of the

159 lithosphere is being removed due to partial melting. In the northwestern and northeastern parts of the study

160 area, the crustal thickness is incomparable. This suggests that the entire lithosphere is being uniformly

161 stretched. Generally, the Hoggar and Tibesti volcanic provinces, which are characterized by negative

162 Bouguer anomalies (Figure 1), are being uplifted in conjunction with lithospheric thinning. The S-wave

163 velocity anomaly images by Abdelslam et al. (2011) show negative shear-wave velocities at depths of

164 100–175 km, suggesting that these anomalies are related to the delamination of a cratonic root.

165   A shallow NVD depth was observed beneath the Hoggar and Tibesti volcanic provinces with a

166 mean of 73 ±10 km (Table 1), which is comparable to the depths beneath the other regions, including the

167 central part of Libya. In the areas adjacent to volcanic provinces, especially beneath the Hoggar volcanic

168 province, the depths of the LAB are the shallowest (62–70 km) in the entire study area, and the crustal

169 thickness is 35 km (Liu and Gao, 2010). The thinning of the lithosphere beneath the Hoggar volcanic

170 province and adjacent areas, such as the Tibesti volcanic province, is consistent with the MTZ thinning

171 hypothesis, which probably originates from the upwelling of hot material from deep sources (Lemnifi et

172 al., 2019). The amount of thinning of the lithosphere is probably proportional to the magnitude of

173 stretching or the amount of partial melt. Our finding is not in agreement with the finding of Liégeois et al.

174 (2005), who used global geophysical modeling and suggested that the lithosphere is relatively thick

175 beneath the Hoggar region.

176   Other areas with a shallow LAB (∼75 km) are the central part of Libya, namely, the Al Haruj and

177 As Sawda volcanic provinces, and the northwestern part of Libya, which is characterized by a crustal

178 thickness of approximately 30 to 35 km (Lemnifi et al., 2017). Marone et al. (2003), Li´egeois et al. (2005),

179 Pasyanos and Nyblade (2007), Montagner et al. (2007), Fishwick (2010), and Bardintzeff et al. (2012)

180 observed negative velocity anomalies beneath the same volcanic provinces from global velocity models.

181 For example, low-velocity zones were noted near depths of 90 km and 107 km in the central part of the

Al Haruj volcanic province. They interpreted that these shallow negative velocity anomalies were probably caused by partial melting. Compared with our lithospheric thickness observations beneath northern Central Africa (62–124 km), the amount of thinning of the subcrustal lithosphere in Fishwick (2010) is comparable. Various studies have suggested that the lithosphere beneath ancient continents (cratons) is thick but widely variable (e.g., Jordan 1975; 1978; Hoffman, 1990; Forte and Perry, 2001). The thick lithosphere beneath Libya (Figure 7) may represent part of the Saharan Metacraton, which extends from the Tuareg Shield to the Arabian-Nubian Shield (Abdelsalam et al., 2002; Lemnifi et al., 2015).

In general, the areas with thin lithosphere have large stacking amplitudes and vice versa (Figure 8). This may suggest that the relationship is attributable to a low degree of partial melting in the topmost layer of the asthenosphere. This is different from other areas, such as the Western United States (Liu and Gao, 2018), which are characterized by a higher degree of partial melting beneath the lithosphere. Here, the degree to which the NVD depths and stacking amplitudes are comparable may reflect a lower degree of partial melting in the topmost asthenosphere and lowermost lithosphere. This may be due to the distance of the study region from the major plate boundaries to the north (e.g., Courtillot et al., 2003).

5. Conclusions

This is the first study to detect the thickness of the lithosphere beneath Central Africa using S-to-P receiver functions (SRFs) recorded by 19 broadband seismic stations. A robust negative-wave speed discontinuity is revealed at depths ranging between 57 km and 110 km with a mean of 80 ±17 km. However, to better understand the variable thickness of the lithosphere beneath the study region, further investigations should be conducted, and additional seismic stations must be installed. Beneath central Libya, the LAB depth ranges from 67 km to 124 km. The smallest LAB depth was found beneath the Hoggar volcanic province, ranging from 57 km to 87 km. One explanation for the observed phenomena is

lithospheric stretching or thinning, which may be due to basal erosion beneath the study region that may be an effect of the LAB topography beneath this part of northern Central Africa.

Acknowledgments

References

Abdelsalam, M. G., Liégeois, J. P., Stern, R. J., 2002. The Saharan Metacraton. J. Afr. Earth Sci. 34, 119–136. https://doi.org/10.1016/S0899-5362(02)00013-1.

Abdelsalam, M.G., Gao, S.S., Ligeois, J.P., 2011. Upper mantle structure of the Saharan Metacraton. J. Afr. Earth Sci. 60, 328–336. https://doi.org/10.1016/j.jafrearsci. 2011.03.009.

Abt, D. L., Fischer, K. M., French, S. W., Ford, H. A., Yuan, H., Romanowicz, B., 2010. NorthAmerican lithospheric discontinuity structure imaged by Ps and Sp receiverfunctions. J. Geophys. Res. 115, B09301.doi:10.1029/2009JB006914.

Anderson, D.L., Spetzler, H., 1970. Partial melting and the low-velocity zone. Phys.Earth Planet. Inter. 4, 62–64.

Bardintzeff, J. M., Deniel, C., Guillou, H., Platevoet, B., T´clouk, P., Oun, K. H., 2012. Miocene to recent alkaline volcanism between Al Haruj and Waw an Namous (southern Libya). J. Inter. Earth Sci. 101, 1047–1063.

Bedle, H., Van Der Lee, S., 2009. S velocity variations beneath North America. J. Geophys. Res. 114(B7).https://doi.org/10.1029/2008JB005949https://doi.org/10.1007/s00531-011-

Caló, M., Bodin, T., Romanowicz, B., 2016. Layered structure in the upper mantle across North America from joint inversion of long and short period seismic data. Earth Planet. Sci. Lett. 499,164–175.https://doi.org/10.1016/j.epsl.2016.05.0540708-5

Cooper, C.M., Lenardic, A., Moresi, L., 2004. The thermal structure of stable continental lithosphere within a dynamic mantle. Earth Planet. Sci. Lett. 222, 807–817

Courtillot, V., Davaille, A., Besse, J., Stock, J., 2003. Three distinct types of hotspots in the Earth's mantle. Earth Planet. Sci. Lett. 205, 295–308. https://doi.org/10.1016/S0012-821X(02)01048-8

234 Dueker, K. G., Sheehan, A. F., 1997. Mantle discontinuity structure from midpoint stacks of converted P
235   to S waves across the Yellowstone hotspot track. J. Geophys. Res.: Solid Earth, 102(B4), 8313-
236   8327.

237 Eaton, D. W., Darbyshire, F., Evans, R. L., Grutter, H., Jones, A. G., Yuan, X., 2009. The elusive
238   lithosphere‐asthenosphere boundary beneath cratons, Lithos, 109,1

239 Faber, S., Müller, G., 1980. Sp phases from the transition zone between the upper and lower mantle. Bull.
240   Seismol. Soc. Am. 70 (2), 487–508.

241 Faul, U. H., Jackson, I., 2005. The seismological signature of temperature and grain size variations in the
242   upper mantle. Earth Planet. Sci. Lett. 234, 119–134.

243 Fischer, K. M., Ford, H. A., Abt, D. L., Rychert, C. A., 2010. The lithosphere-asthenosphere boundary.
244   Annu. Rev. Earth Planet. Sci., 38, 551‐575, doi:10.1146/annurev-earth-040809-152438.

245 Fishwick, S., 2010. Surface wave tomography: Imaging of the lithosphere asthenosphere boundary
246   beneath central and southern Africa? Lithos,120(1),63–73.
247   https://doi.org/10.1016/j.lithos.2010.05.011

248 Gao, S. S., Liu, K. H., 2014. Mantle transition zone discontinuities beneath the contiguous United States.
249   J. Geophys. Res.: Solid Earth, 119(8), 6452-6468.

250 Kennett, B. L. N., Engdahl, E. R., 1991. Traveltimes for global earthquake location and phase
251   identification: J. Geophys. Inter. 105, 429–465, doi: 10 .1111 /j.1365 -246X.1991.tb06724 .x.

252 Kind, R.,Yuan, X., Kumar, P., 2012. Seismic receiver functions and the lithosphere-asthenosphere
253   boundary. Tectonophysics 536, 25–43. https://doi.org/10.1016/j.tecto.2012.03.005.

254 King, S.D., Ritsema, J., 2000. African hot spot volcanism: small-scale convection in the upper mantle
255   beneath cratons. Science 290, 1137–1140.

256 Korenaga, J., Jordan, T.H., 2002. On the state of sublithospheric upper mantle beneath a supercontinent.
257   J. Geophys. Int. 149, 179–189.

258 Lee, C. T. A., 2003. Compositional variation of density and seismic velocities in naturalperidotites at STP
259   conditions: implications for seismic imaging of compositional heterogeneities in the upper mantle.
260   J. Geophys. Res. 108. doi:10.1029/2003JB002413.

261 Lemnifi, A.A., Liu, K.H., Gao, S.S., Reed, C.A., Elsheikh, A.A., Yu, Y., Elmelade, A.A., 2015. Azimuthal
262   anisotropy beneath north central Africa from shear wave splitting analyses. Geochem. Geophys.
263   Geosyst. 16. https://doi.org/10.1002/2014GC005706.

264 Lemnifi, A., Elshaafi, A., Browning, J., Aouad, N., El Ebadi, S., Liu, K., Gudmundsson, A., 2017. Crustal
265   thickness beneath Libya and the origin of partial melt beneath AS Sawda Volcanic Province from
266   receiver- function constraints. J. Geophys. Res. Solid Earth.
267   https://doi.org/10.1002/2017JB014291.

268 Lemnifi, A., Browning, A., Elshaafi, A., Aouad, N., Yu, Y., 2019. Receiver function imaging of mantle
269   transition zone discontinuities and the origin of volcanism beneath Libya. J. Geodynamics, 93-
270   103. https://doi.org/10.1016/j.jog.2019.01.009.

271 Liégeois, J. P., Benhallou, A., Azzouni-Sekkal, A., Yahiaoui, R., Bonin, B., 2005. The Hoggar swell and
272   volcanism: Reactivation of the Precambrian Tuareg shield during Alpine convergence and West
273   African   Cenozoic   volcanism.   Geolog.   Soci.   Amer.,   Special   Papers,388,379–
274   400.https://doi.org/10.1130/0-8137-2388-4.379.

275 Liu, K. H., Gao, S. S., 2010. Spatial variations of crustal characteristics beneath the Hoggar swell, Algeria,
276   revealed by systematic analyses of receiver functions from a single seismic station. Geochem.
277   Geophys. Geosyst. 11(8). http://doi.org/10.1029/2010GC003091

278 Liu, L., Gao, S. S., Liu, K. H., Mickus, K., 2017. Receiver function and gravity constraints on crustal
279   structure and vertical movements of the Upper Mississippi Embayment and Ozark Uplift. J.
280   Geophys. Res. 122,4572–4583.https://doi.org/10.1002/2017JB014201

281 Liu, L., Gao, S., 2018. Lithospheric layering beneath the contiguous United States constrained by S-to-P
282   receiver functions. Earth Planet. Sci. Lett. 495, 79–86.

283 Marone, F., Van Der Meijde, M., Van Der Lee, S., Giardini, D., 2003. Joint inversion of local, regional
284   and teleseismic data for crustal thickness in the Eurasia-Africa plate boundary region. J. Geophys.
285   Intern. 154 (2), 499–514. https://doi.org/10.1046/j. 1365-246X.2003.01973.x.

286 McKenzie, D., Priestley, K., 2008. The influence of lithospheric thickness variations on continental
287   evolution. Lithos 102(1),1–11.https://doi.org/10.1016/j.lithos.2007.05.005

288 Montagner, J.-P., et al., 2007. Mantle upwellings and convective instabilities revealed by seismic
289   tomography and helium isotope geochemistry beneath eastern Africa. Geophys. Res. Lett.
290   https://doi.org/10.10129/2007GL031098. L21303.

291 Parsons, T., Thompson, G. A., Sleep, N. H., 1994. Mantle plume influence on the Neogene uplift and
292   extension of the US western Cordillera? Geology 22, 83–86.

293 Pasyanos, M. E., Nyblade, A. A., 2007. A top to bottom lithospheric study of Africa and Arabia.
294   Tectonophysics, 444, 27–44. https://doi.org/10.1016/j.tecto.2007.07.008.

295 Priestley, K., McKenzie, D., 2006. The thermal structure of the lithosphere from shear wave velocities.
296   Earth Planet. Sci. Lett., 244, 285–301, doi:10.1016/j.epsl.2006.01.008.

297 Rychert, C. A., Shearer, P. M., 2009. A global view of the lithosphere-asthenosphere boundary. Science,
298   324, 495 –498, doi:10.1126/ science.1169754.

299 Schaeffer, A. J., Lebedev, S., 2014. Imaging the North American continent using wave form inversion of
300   global   and   US   Array   data.   Earth   Planet.   Sci.   Lett.   402,26-41.
301   https://doi.org/10.1016/j.epsl.2014.05.014.

302 Schutt, D. L., Lesher, C. E., 2006. Effects of melt depletion on the density and seismic velocity of garnet
303   and spinel lherzolite, J. Geophys. Res., 111, B05401, doi:10.1029/2003JB002950.

304 Sheriff, R. E., Geldart, L. P., 1982. Exploration Seismology. Vol.1: History, Theory, and Data Acquisition.
305   Cambridge University Press, Cambridge.

306 Stixrude, L., Lithgow-Bertelloni, C., 2005. Mineralogy and elasticity of the oceanic upper mantle: origin
307   of the low-velocity zone. J. Geophys. Res. 110. doi:10.1029/2004JB002965.

308 Yuan, X., Kind, R., Li, X., Wang, R., 2006. The S receiver functions: synthetics and data example. J.
309   Geophys. Inter. 165(2), 555-564.

310 Yuan, H., Romanowicz, B., 2010. Lithospheric layering in the North American Craton. Nature 466, 1063–
311   1068.

312 Zhu, L. P., Kanamori, H., 2000. Moho depth variation in southern California from teleseismic receiver
313   functions, J. Geophys. Res., 105, 2969‑2980, doi:10.1029/1999JB900322.

314

315

316

317

318

319

320

321

322
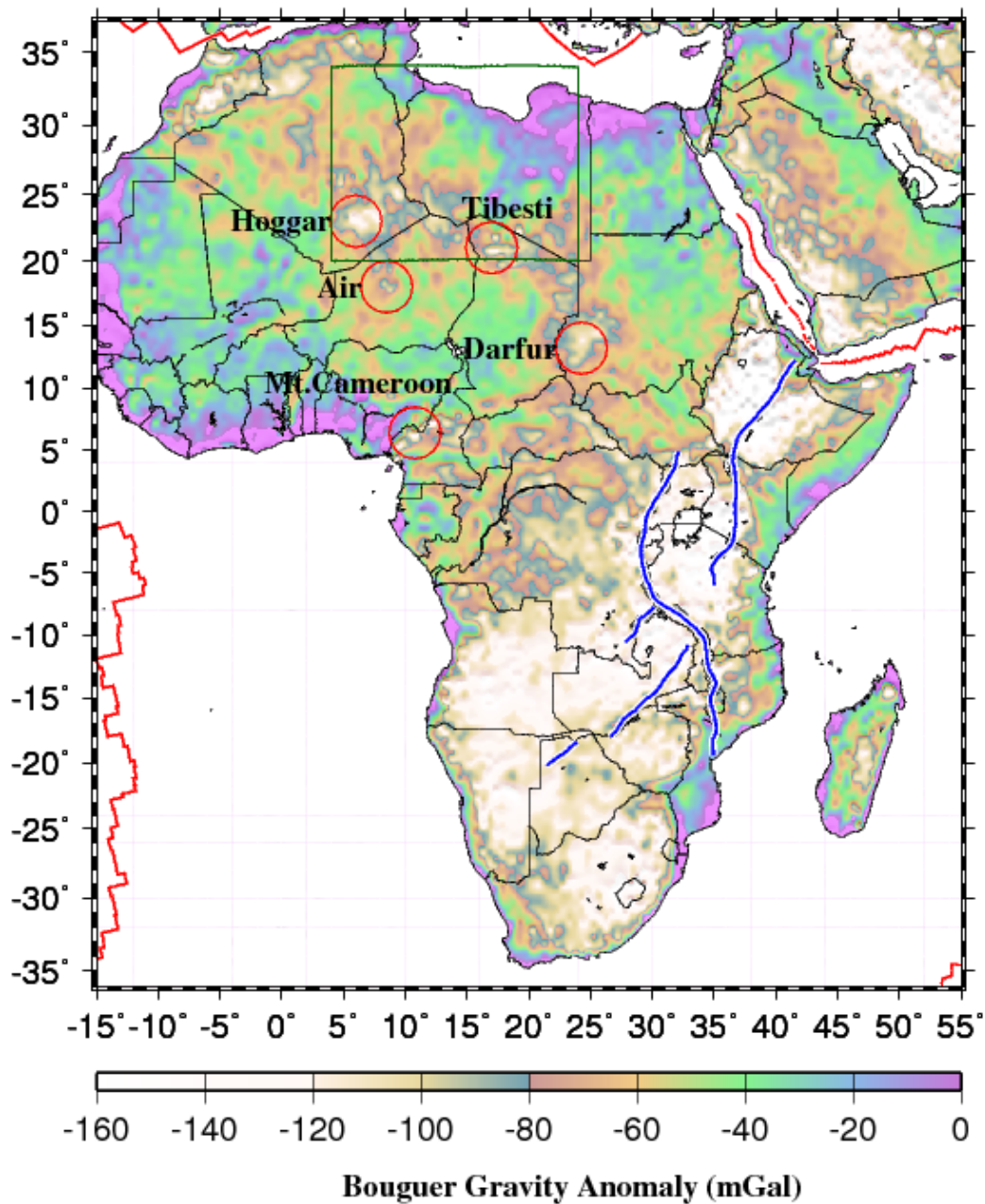
Figure 1. Map of the Bouguer gravity anomalies throughout Africa produced using GRACE (Gravity Recovery and Climate Experiment) satellite gravity data (Tapley et al., 2005; Liu and Gao, 2010). The blue lines illustrate the East African Rift System. The green square denote the location of the study area. The circles are centered on the major Cenozoic volcanic provinces of Africa.
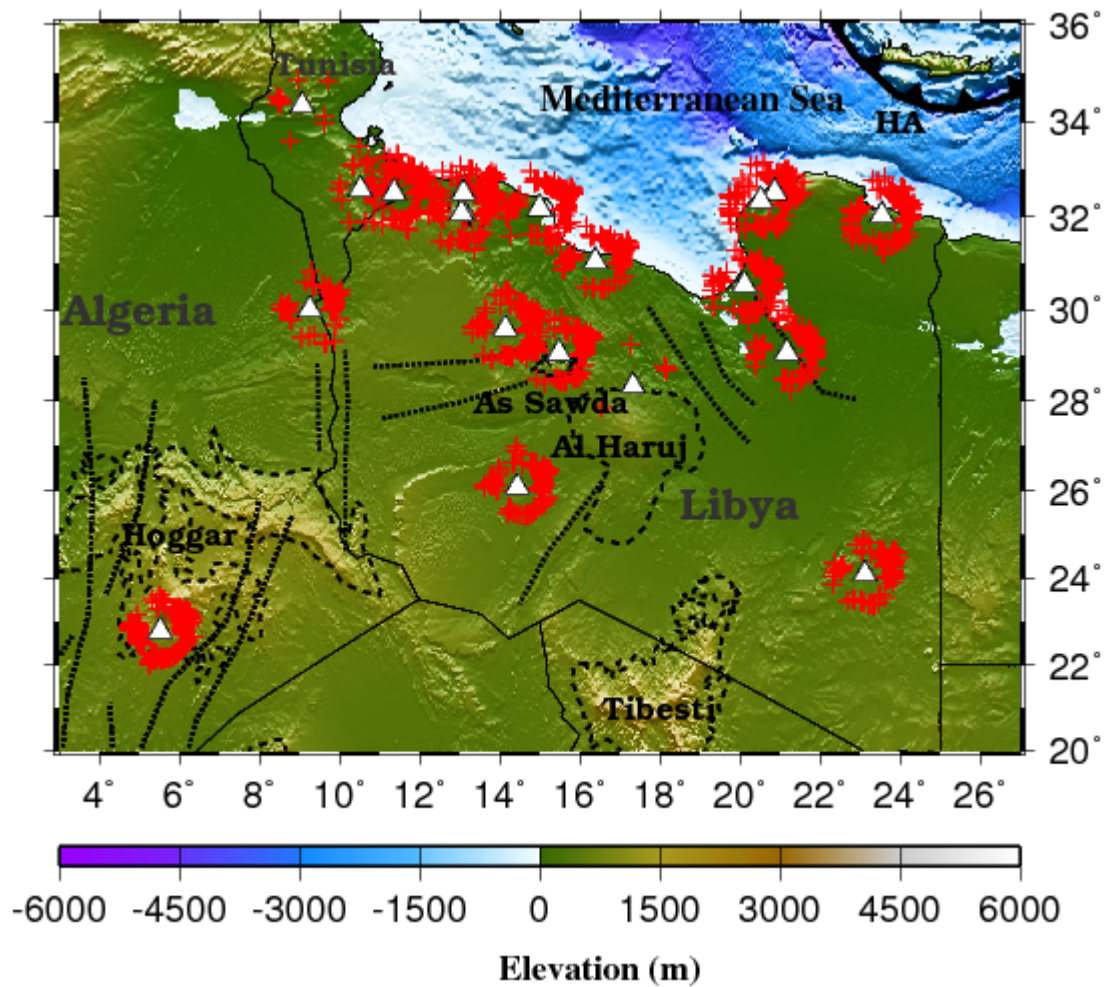
Figure 2. Digital elevation map of the study area showing the seismic stations used in the study. Crosses are the ray-piercing points at a depth of 150 km. Black dashed lines surround the major volcanic provinces in the study area.
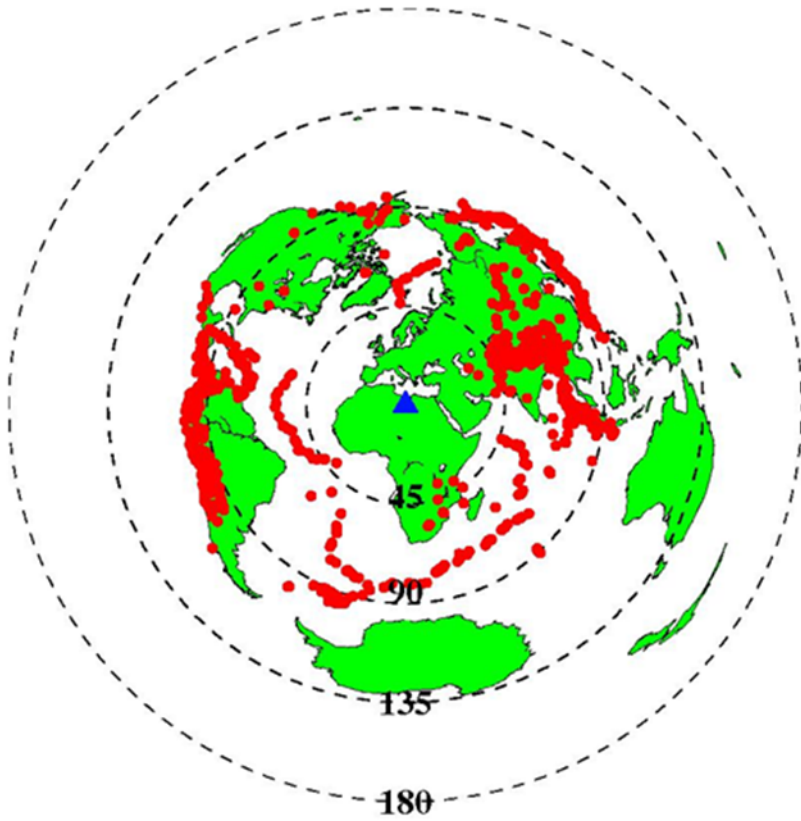
Figure 3. An azimuthal equidistant projection map showing the distribution of earthquakes (red dots) used for the receiver function analysis.

Figure 4. Diagram showing the number of RFs in radius=2 degree bins. The color scale represents the number of RFs per bin.
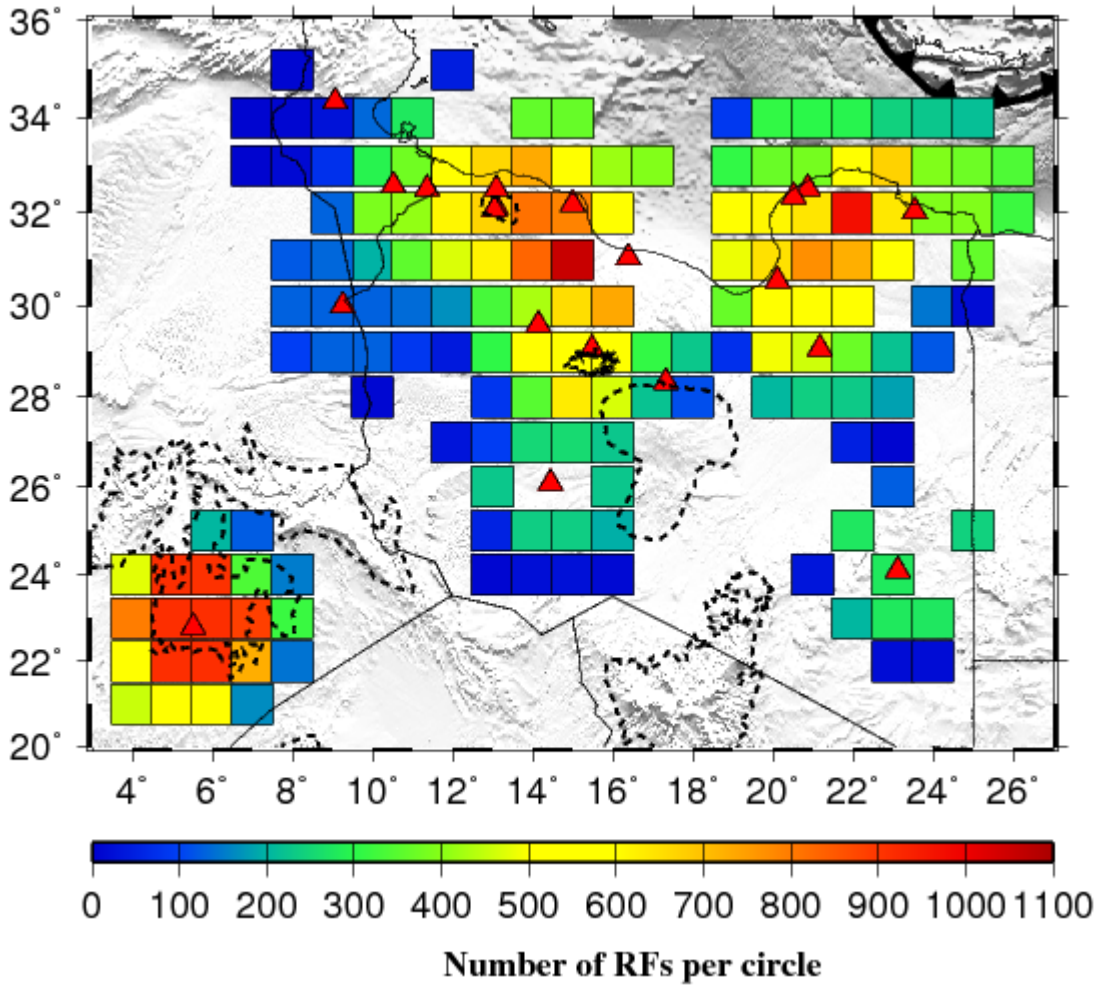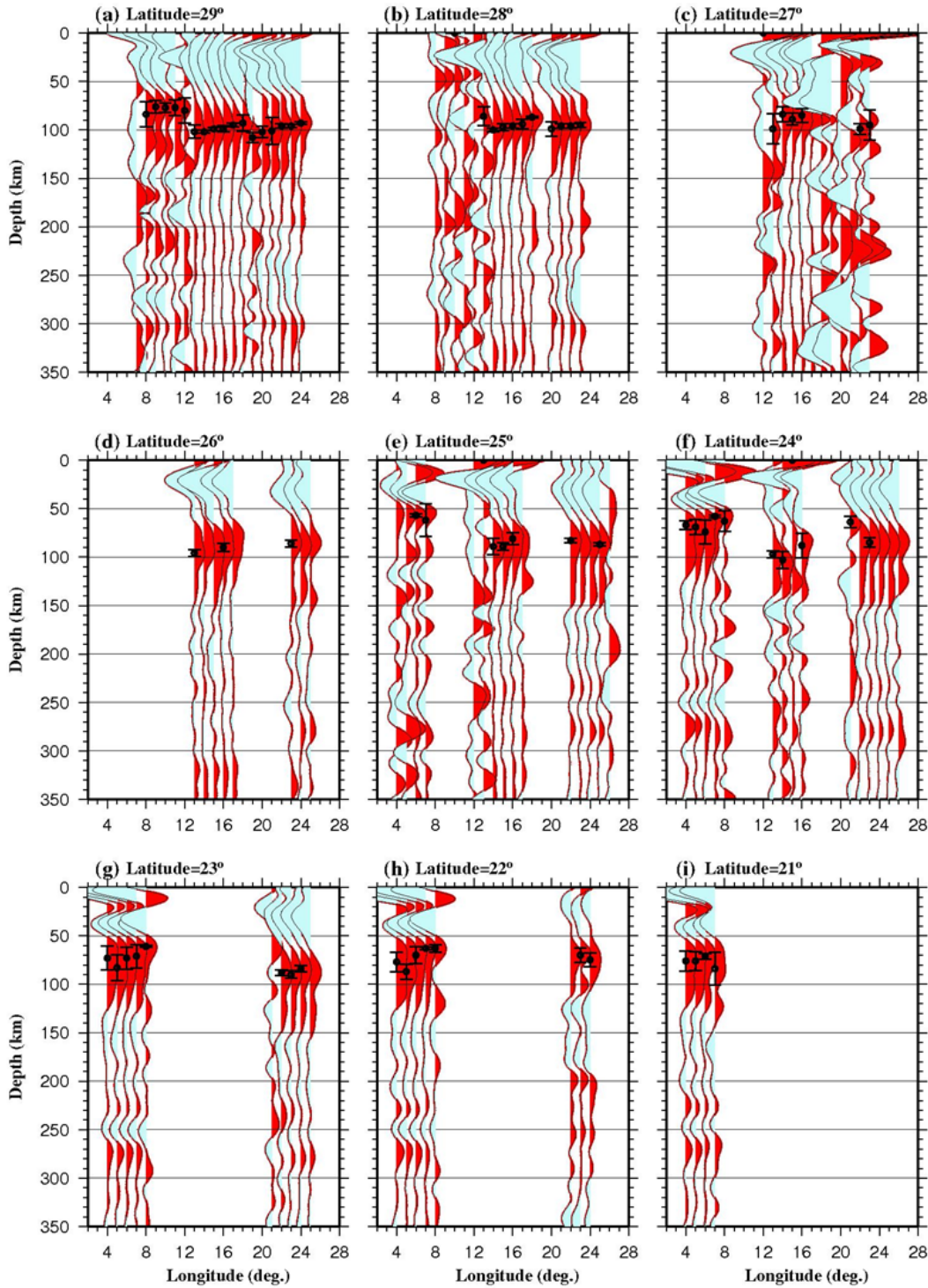
Figure 5. E-W stacked S-to-P receiver function profiles showing the depths from 0 to 350 km at latitudes from 21°N to 29°N. Black circles represent the average depths of the LAB, and black bars show two STDs of the peak depths.

345
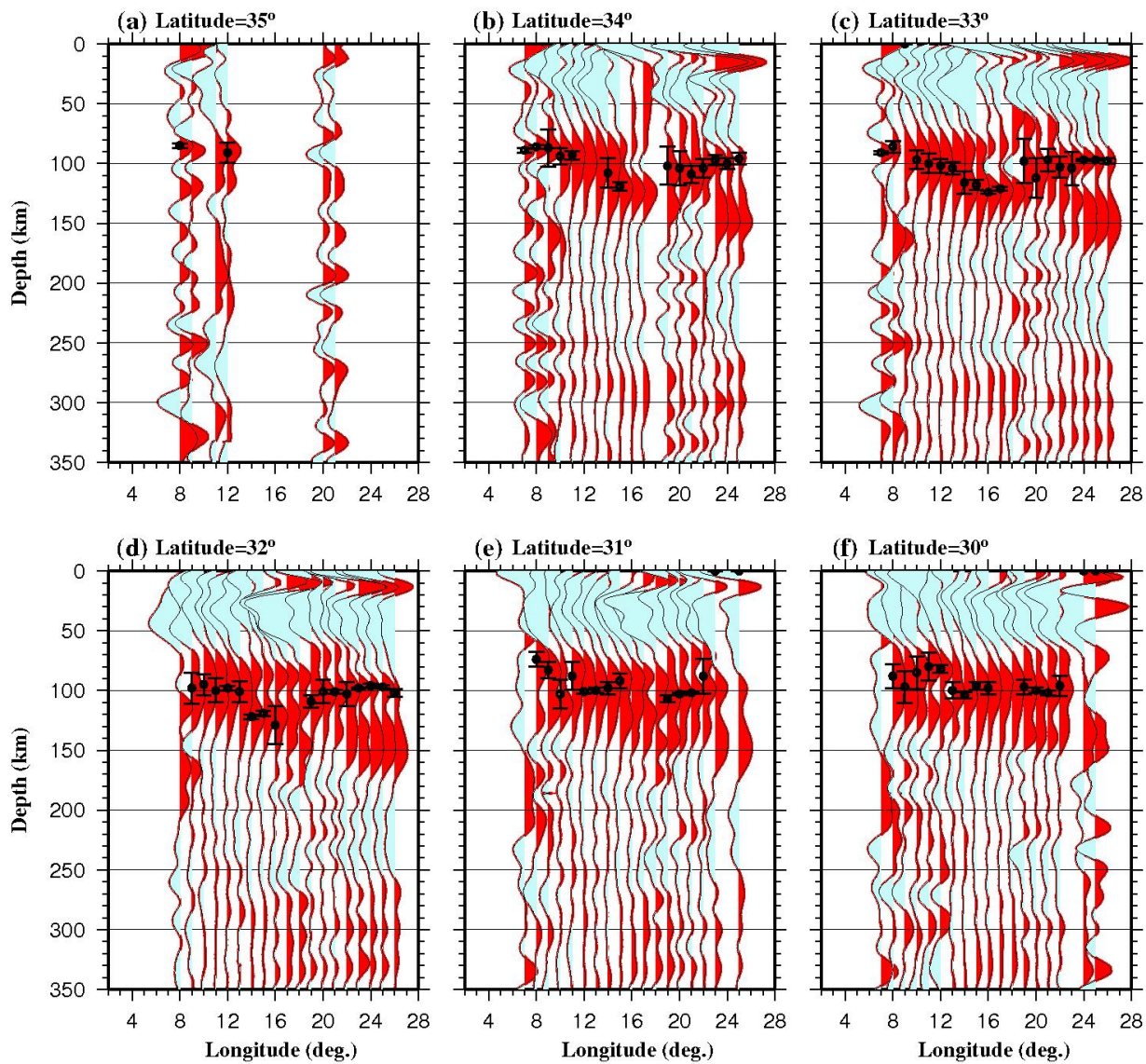
Figure 6. Same as Figure 5 but showing the profiles from 30°N to 35°N. Black circles represent the average

depths of the LAB, and black bars show two STDs of the peak depths.

349
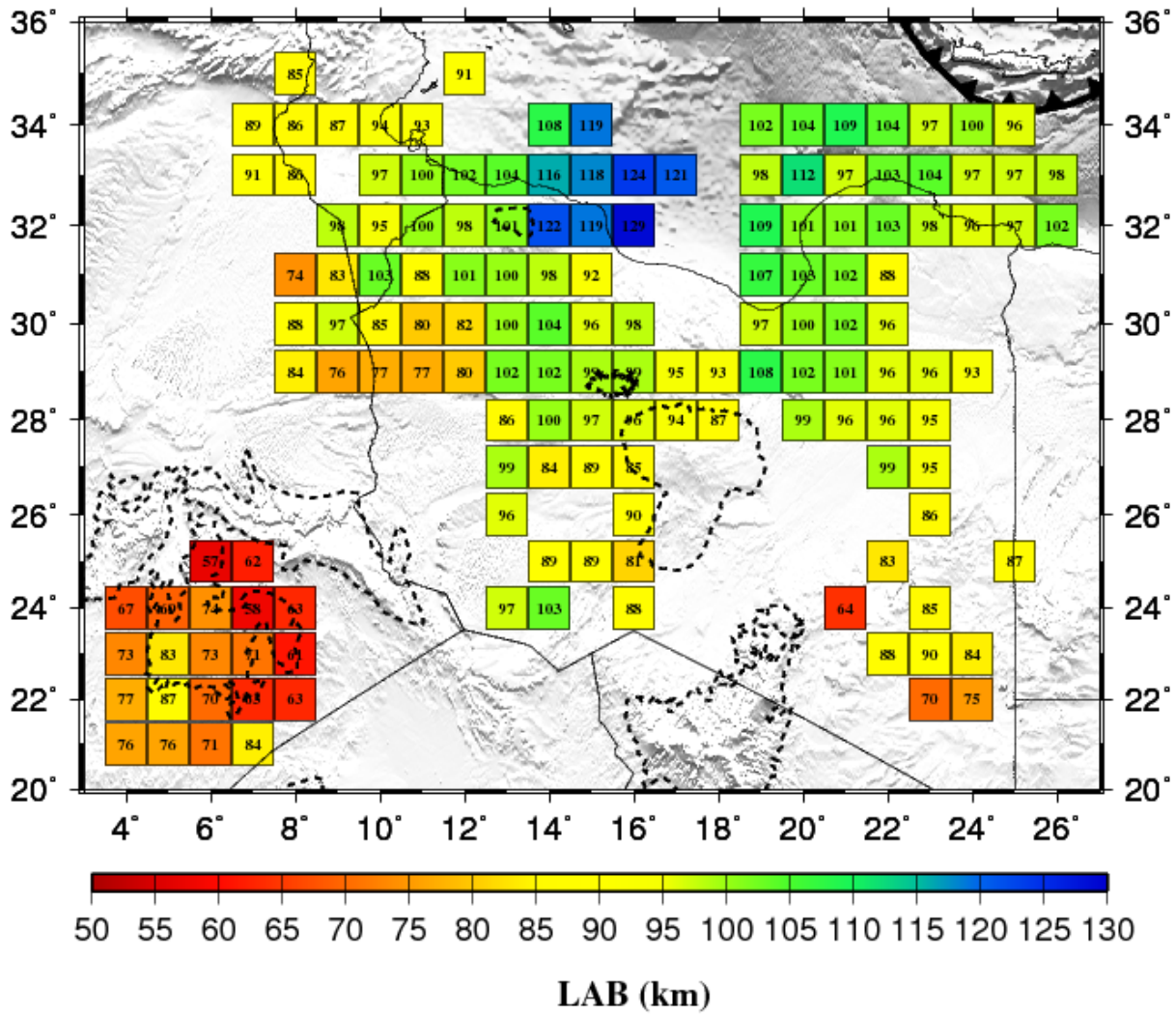
Figure 7. Diagram showing the resulting depth of the LAB throughout the study area. The colours represent the LAB depths from 50 to 130 km, where the mean depth is also given in each locality.
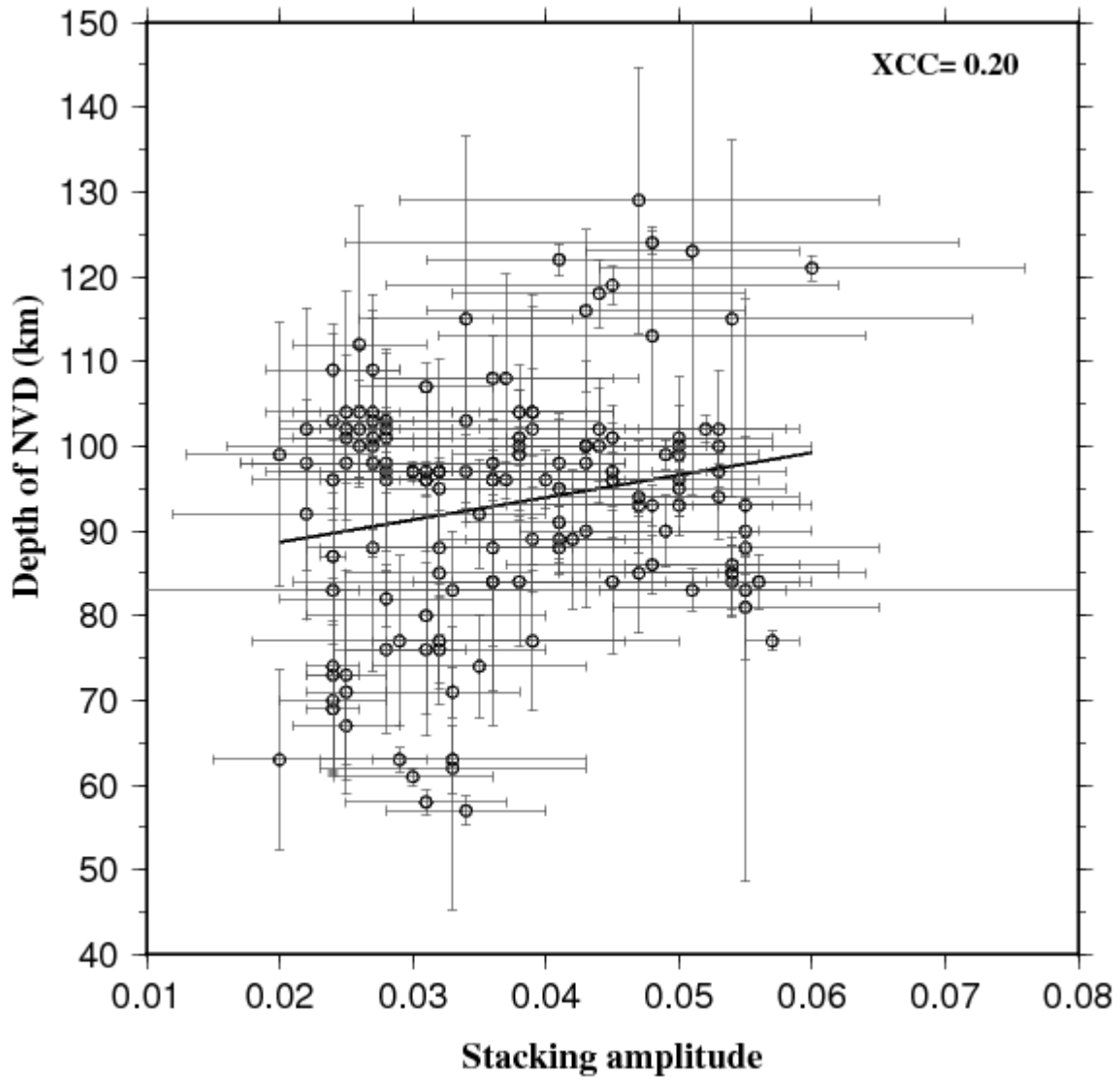
353

354   Figure 8. Cross-correlation plot of the NVD depths versus the corresponding stacking amplitudes.

355

356

357

358

359   Table. 1. Resulting NVD depths and stacking amplitudes.

Longitude	Latitude	Depth of NVD (km)	Stacking amplitude of NVD	Number of SRFs
6.00	25.00	57	0.034	203
7.00	24.00	58	0.031	338
8.00	23.00	61	0.030	317
7.00	25.00	62	0.033	123
8.00	24.00	63	0.020	151
7.00	22.00	63	0.029	727
8.00	22.00	63	0.033	143
4.00	24.00	67	0.025	477
5.00	24.00	69	0.024	914
6.00	22.00	70	0.024	914
6.00	21.00	71	0.033	571
7.00	23.00	71	0.025	887
4.00	23.00	73	0.025	797
6.00	23.00	73	0.024	914
6.00	24.00	74	0.024	910
8.00	31.00	74	0.035	121
5.00	21.00	76	0.028	590
4.00	21.00	76	0.031	454
9.00	29.00	76	0.032	128
4.00	22.00	77	0.029	585
11.00	29.00	77	0.039	85
17.00	26.00	77	0.057	175
10.00	29.00	77	0.032	128
11.00	30.00	80	0.031	136
16.00	25.00	81	0.055	195
12.00	30.00	82	0.028	168

5.00	23.00	83	0.024	914
18.00	33.00	83	0.055	125
22.00	25.00	83	0.051	275
9.00	31.00	83	0.033	133
7.00	21.00	84	0.036	165
24.00	25.00	84	0.054	279
24.00	23.00	84	0.056	275
14.00	27.00	84	0.038	251
8.00	29.00	84	0.036	94
17.00	27.00	84	0.045	161
22.00	24.00	85	0.054	279
10.00	30.00	85	0.032	128
23.00	24.00	85	0.054	279
25.00	26.00	85	0.091	50
16.00	27.00	85	0.047	226
24.00	24.00	86	0.054	279
23.00	26.00	86	0.048	125
25.00	24.00	86	0.063	253
5.00	22.00	87	0.024	914
18.00	28.00	87	0.061	111
25.00	23.00	87	0.068	232
25.00	25.00	87	0.065	242
22.00	31.00	88	0.027	726
11.00	31.00	88	0.036	356
8.00	30.00	88	0.032	128
24.00	26.00	88	0.069	225
22.00	23.00	88	0.041	203
23.00	25.00	88	0.055	279

15.00	27.00	89	0.039	256
15.00	25.00	89	0.041	236
14.00	25.00	89	0.042	236
23.00	23.00	90	0.055	279
15.00	26.00	90	0.043	237
16.00	26.00	90	0.049	226
14.00	26.00	91	0.041	238
15.00	31.00	92	0.035	1056
13.00	28.00	92	0.022	81
24.00	29.00	93	0.047	119
17.00	30.00	93	0.048	539
18.00	29.00	93	0.055	227
11.00	34.00	93	0.050	277
10.00	34.00	94	0.047	134
17.00	28.00	94	0.053	220
10.00	32.00	95	0.041	387
23.00	28.00	95	0.032	183
18.00	30.00	95	0.050	392
17.00	29.00	95	0.061	310
13.00	26.00	96	0.040	227
22.00	29.00	96	0.031	369
22.00	30.00	96	0.028	523
16.00	28.00	96	0.050	467
21.00	28.00	96	0.036	238
22.00	28.00	96	0.037	231
25.00	34.00	96	0.024	215
23.00	29.00	96	0.036	220
15.00	30.00	96	0.045	653

24.00	32.00	96	0.031	393
23.00	34.00	97	0.034	242
19.00	30.00	97	0.028	366
10.00	33.00	97	0.045	294
24.00	33.00	97	0.032	393
25.00	33.00	97	0.030	372
21.00	33.00	97	0.031	381
25.00	32.00	97	0.030	393
15.00	28.00	97	0.053	631
9.00	30.00	97	0.032	128
19.00	33.00	98	0.022	308
16.00	30.00	98	0.041	736
14.00	31.00	98	0.036	832
26.00	33.00	98	0.025	339
12.00	32.00	98	0.043	614
9.00	32.00	98	0.028	129
23.00	32.00	98	0.027	637
16.00	29.00	99	0.050	512
20.00	28.00	99	0.038	204
15.00	29.00	99	0.049	531
13.00	27.00	99	0.020	92
20.00	30.00	100	0.027	542
11.00	33.00	100	0.050	376
12.00	34.00	100	0.053	375
13.00	31.00	100	0.038	620
14.00	28.00	100	0.043	349
11.00	32.00	100	0.043	409
13.00	30.00	100	0.044	331

24.00	34.00	100	0.026	226
13.00	34.00	101	0.050	440
21.00	29.00	101	0.027	459
20.00	32.00	101	0.025	615
12.00	31.00	101	0.045	469
13.00	32.00	101	0.038	670
21.00	32.00	101	0.028	641
21.00	30.00	102	0.028	550
19.00	34.00	102	0.039	86
14.00	29.00	102	0.052	515
13.00	29.00	102	0.053	305
21.00	31.00	102	0.025	772
26.00	32.00	102	0.022	319
20.00	29.00	102	0.026	491
12.00	33.00	102	0.044	597
22.00	33.00	103	0.028	556
20.00	31.00	103	0.027	649
22.00	32.00	103	0.024	974
10.00	31.00	103	0.034	198
20.00	34.00	104	0.025	309
16.00	31.00	104	0.039	912
13.00	33.00	104	0.039	665
22.00	34.00	104	0.026	295
14.00	30.00	104	0.038	429
23.00	33.00	104	0.027	673
19.00	31.00	107	0.031	485
19.00	29.00	108	0.036	72
14.00	34.00	108	0.037	361

21.00	34.00	109	0.027	301
19.00	32.00	109	0.024	577
20.00	33.00	112	0.026	368
17.00	31.00	113	0.048	479
17.00	32.00	115	0.054	459
18.00	31.00	115	0.034	285
14.00	33.00	116	0.043	733
15.00	33.00	118	0.044	590
15.00	32.00	119	0.045	789
15.00	34.00	119	0.076	365
17.00	34.00	121	0.188	85
17.00	33.00	121	0.060	395
14.00	32.00	122	0.041	815
16.00	34.00	123	0.102	216
18.00	32.00	123	0.051	298
16.00	33.00	124	0.048	417
16.00	32.00	129	0.047	563
11.00	35.00	140	0.076	49

360